

Device-Level Parallel-in-Time Simulation of MMC-Based Energy System for Electric Vehicles

Chengzhang Lyu , *Graduate Student Member, IEEE*, Ning Lin , *Member, IEEE*,
and Venkata Dinavahi , *Fellow, IEEE*

Abstract—The device-level electromagnetic transient (EMT) simulation with the nonlinear behaviour model (NBM) of insulated-gate bipolar transistors (IGBTs) and diodes can provide an accurate insight into the power converters from the perspective of thermal performance and energy efficiency. However, device-level simulation is rarely implemented in electric vehicles (EVs) due to its extreme computation complexity natively introduced by the device models. To solve this problem, an interpolation strategy is designed based on the parallel-in-time algorithm for the device-level simulation of the modular multilevel converter (MMC) connected with the induction machine in EV applications. The MMC is mathematically separated as multiple submodules with the same attributes, which can be processed in a parallel manner in the graphics processing unit (GPU). By implementing the device-level simulation in the different time-step in GPU, the interpolation strategy provides the precise initial values for the nonlinear solution process iteratively. The accuracy of the proposed simulation scheme is validated by commercial simulation tools at the device level. In addition, the system-level simulation of EVs is carried out at different driving cycles, and the results demonstrate a significant reduction in simulation time.

Index Terms—Device-level electromagnetic transient simulation, nonlinear behaviour model, graphics processors, modular multilevel converter, parallel processing, electric vehicles.

I. INTRODUCTION

GROWING concerns about environmental protection against exhaust emission have drawn more attention to electric vehicles (EVs) [1], [2]. Induction machines (IMs), known to have a robust structure and efficient energy conversion, are widely used in commercial EVs [3]. Thus, it is of vital importance to develop efficient three-phase drives for IM to enhance system performance [4], [5]. Due to the highly modular structure, low switching power consumption, solid harmonic suppression, and inherently bidirectional characteristic, the modular multilevel converter (MMC) is a potential candidate for IM-based EVs [2], [5]–[7].

Nevertheless, MMC implementation brings new challenges to the design and testing of EVs; it is essential to improve the

EV simulation technology to reveal the insight into MMC and IM, specifically at the early design period [8], [9]. Most EV research focuses on the energy management strategy [10]–[13] and battery charging [14], [15]; however, seldom on the device-level simulation for EVs. Thus, the electromagnetic transient (EMT) simulation is developed in this paper to embed both the system-level and the device-level simulation into the energy system of EVs.

The models of IGBT and power diodes are crucial to device-level simulation accuracy. Generally, the ideal model, the analytical model [16], [17] and the nonlinear behaviour model (NBM) [18] are widely used for the EMT simulation of IGBT and diode. The ideal model cannot represent the transient period of IGBT and diode. The one-dimension model was reviewed in [16] from the perspective of the ON-state characteristics and switching behaviour. A three-dimension thermal network of IGBT was developed in [17] for the high-power IGBT modules. However, the analytical model involves complex nonlinear physical equations into the solution process, which is too burdensome for computing processors. Nonlinear behavioural models (NBMs) have lower complexity by circumventing the detailed physical characteristics and can also provide an accurate prediction of converter performance, including temperature, switch stresses, and etc., which are currently prevalent in EMT tools [18].

Furthermore, the onboard lithium-ion batteries and power-train are significantly concerned in the design and assessment of the EV's energy system. In consequence, the system-level simulation of EVs suffers from the extreme computation burden as those device-level models bring the high complexity into the system ordinary differential equation (ODE) [19]. Recently, the parallel-in-time algorithm is a potential alternative to accelerate the nanosecond-level simulation [20]. In [21], the parallel-in-time algorithm is implemented with detailed models for accelerating the power systems simulation, in which more precious initial values are provided in order to reduce the nonlinear iteration numbers. In [22], a sequential program based on a parallel-in-time algorithm is proposed to solve the semi-explicit differential-algebraic equations system of the power dynamic simulation problem.

In this paper, the device-level parallel-in-time simulation scheme is designed for EVs to reveal the MMC-based energy system's insight and performance. In particular, a modified interpolation strategy is designed based on the parallel-in-time algorithm to achieve the twofold goals of both high accuracy

Manuscript received January 1, 2021; revised April 9, 2021; accepted May 11, 2021. Date of publication May 18, 2021; date of current version July 8, 2021. This work was supported by the Natural Science and Engineering Research Council (NSERC) of Canada. The work of Chengzhang Lyu was supported by the China Scholarship Council. The review of this article was coordinated by Dr. Mehdi Narimani. (*Corresponding author: Chengzhang Lyu.*)

The authors are with the Department of Electrical and Computer Engineering, University of Alberta, Edmonton, AB T6G 2V4, Canada (e-mail: clyu1@ualberta.ca; ning3@ualberta.ca; dinavahi@ualberta.ca).

Digital Object Identifier 10.1109/TVT.2021.3081534

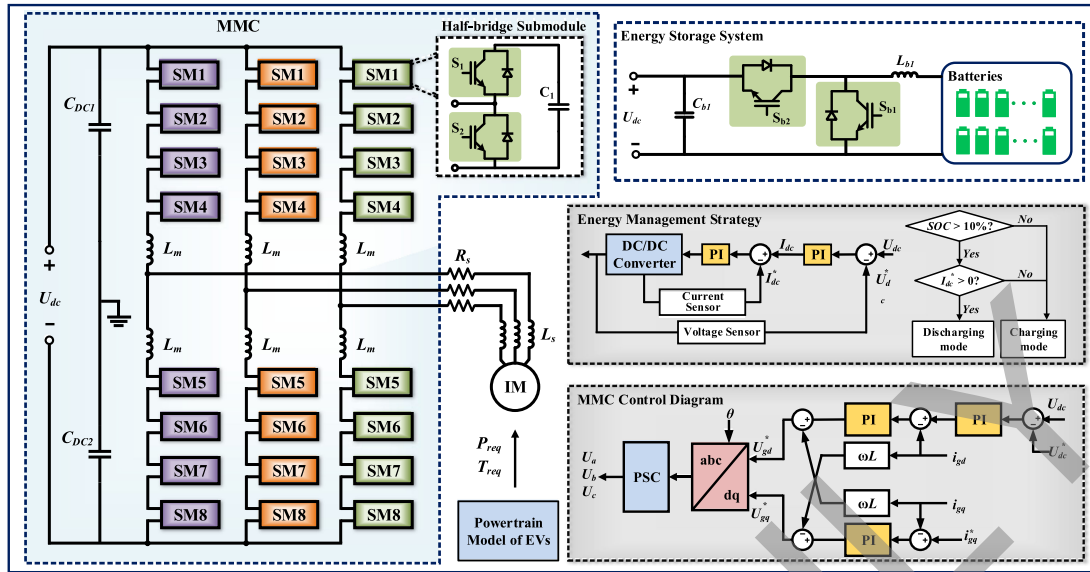


Fig. 1. EV power system used for transient simulation.

and low time consumption of both device-level and system-level simulation of the EVs. First, the NBM is implemented to expose the dynamic characteristics of the IGBT and the diode. The MMC is mathematically separated as submodules to reduce the system matrix complexity. Second, the batteries state-of-charge (SOC) model and the IM model are implemented to build the energy and power relationship between the power converters and the energy systems. Third, an interpolation strategy is designed based on the parallel-in-time algorithm with the coarse operator and the precise operator. The coarse operator's solution is provided to the precise operator as the estimated initial value iteratively, which can alleviate the increasing nonlinear iteration times for solving device-level models. The device-level model is validated in Synopsys SaberRD, which is widely used in EMT simulation and EV applications [23]–[25]. The system-level simulation is accomplished in the MMC-based energy system of a Tesla Model EV under different driving cycles in the graphics processing unit (GPU) environment. Simulation results that the proposed interpolation strategy significantly reduces simulation time consumption.

This paper is organized as follows. Section II introduces the third-order resistance-capacitance (RC) battery model, IM model, and NBM of IGBTs and diodes. The MMC-based energy system, including the powertrain model of the EVs, is discussed in Section III. The proposed parallel-in-time interpolation strategy is designed in Section IV. Simulation results are shown in Section V, and Section VI provides conclusions.

II. DEVICE-LEVEL MODELING OF EV ENERGY SYSTEM

The device-level EMT simulation scheme of EV is demonstrated in Fig. 1, which mainly composes of the powertrain model, the battery-based energy storage system, and the MMC inverter connected with the IM along with the corresponding control system. In this case, the state-of-charge (SOC) model is required to indicate the remaining energy of the energy storage

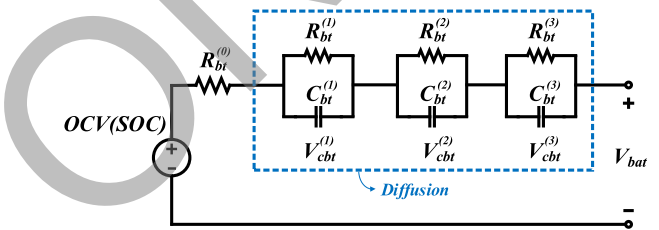


Fig. 2. Equivalent circuit of third-order RC model of the battery.

system. In addition, The models of the IM, the IGBTs and diodes are necessary for the EMT device-level simulation. In this work, the NBM model of IGBTs and diodes is adopted to provide accurate insights into power switches. The IM model is implemented for the voltage requirements of MMC.

A. Battery State-of-Charge Modeling

Batteries play an important role in EV as the energy supply. Based on the purpose of device-level simulation, a battery model is required to represent the relationship between battery voltage and energy storage [15]. The third-order RC equivalent circuit model of the Li-ion battery is shown in Fig. 2. R_{bat}^0 represents the equivalent resistance of battery at steady state, while the chemical diffusion behaviour of the electrolyte and the inner resistance of the battery is modeled by the three branches [26]. The voltage source represents the internal charge transfer process provided by the electrochemical reaction of electrolyte and anode materials. Based on Kirchhoff's laws, the relationship between the open-circuit voltage (OCV) of an inner voltage source and battery voltage V_{bt} takes the form of

$$V_{bt} = OCV(SOC) + I_{bt}R_{bt}^{(0)} + \sum_{i=1}^3 V_{C_{bt}}^{(i)}, \quad (1)$$

where $V_{C_{bt}}^{(i)}$ is the voltage across $C_{bt}^{(i)}$.

TABLE I
 PARAMETERS OF BATTERY SOC MODEL

SOC	10% - 20%	20% - 30%	30% - 40%	40% - 50%
a_{bat}	0.0049	0.0039	0.0028	0.0036
b_{bat}	3.5188	3.5397	3.5728	3.5416
SOC	50% - 60%	60% - 70%	70% - 80%	80% - 90%
a_{bat}	0.006	0.0082	0.008	0.009
b_{bat}	3.4199	3.2864	3.3004	3.2232

The relationship between OCV and SOC is nonlinear so that OCV cannot perform accurately as the mathematical interpretation for SOC. Considering both the computation complexity and accuracy, the SOC can be obtained from a piecewise function [27],

$$OCV(SOC) = a_{bt}SOC + b_{bt}, \quad (2)$$

where a_{bt} and b_{bt} are the parameters of the SOC estimation, which are listed in Tab I. Since the depth of discharge of the battery is 80% (from 10% to 90%), the piecewise function is divided into 8 subsections.

The battery SOC is basically defined as the ratio of the remaining energy over the nominal energy capacity. The error between the approximated values and experimental results is acceptable for the device-level simulation. The maximum voltage error of the third-order RC model is 0.2 % [26], while the maximum SOC error is around 2 % when the initial SOC is given [27].

B. Induction Machine Modeling

The IM is favored in EV due to their ruggedness and simplicity. Furthermore, the IM is the core device that converts the batteries energy into electricity for driving EVs.

In this work, the equivalent circuit model of IM is adopted for the IM modeling, according to [28]. The state-space equations of IM model are available as

$$\begin{aligned} \hat{\mathbf{X}}_{IM} &= \mathbf{A}_{IM}\mathbf{X}_{IM} + \mathbf{B}_{IM}\mathbf{U}_{IM}, \\ \mathbf{I}_{IM} &= \mathbf{C}_{IM}\mathbf{X}_{IM}, \end{aligned} \quad (3)$$

where \mathbf{X}_{IM} is the vector of fluxes, \mathbf{I}_{IM} is the currents, and \mathbf{U}_{IM} is excitations in the α - β frame. The state variables are denoted by $\mathbf{X}_{IM} = [X_{\alpha s}, X_{\beta s}, X_{\alpha r}, X_{\beta r}]^T$, where the subscript s and r are the short form of the variables belonging to the stator or rotor, respectively. The state matrix is defined as

$$\mathbf{A}_{IM} = \begin{bmatrix} \frac{-R_s L_r}{L_{IMeq}} & 0 & \frac{R_s L_m}{L_{IMeq}} & 0 \\ 0 & \frac{-R_s L_r}{L_{IMeq}} & 0 & \frac{R_s L_m}{L_{IMeq}} \\ \frac{R_r L_m}{L_{IMeq}} & 0 & \frac{-R_r L_m}{L_{IMeq}} & -\omega_r \\ 0 & \frac{R_r L_m}{L_{IMeq}} & \omega_r & \frac{-R_r L_m}{L_{IMeq}} \end{bmatrix}, \quad (4)$$

where the equivalent inductance $L_{IMeq} = L_s L_r - L_m^2$, and output matrix is

$$\mathbf{C}_{IM} = \begin{bmatrix} \frac{L_r}{L_{IMeq}} & 0 & \frac{-L_m}{L_{IMeq}} & 0 \\ 0 & \frac{L_r}{L_{IMeq}} & 0 & \frac{-L_m}{L_{IMeq}} \\ \frac{-L_m}{L_{IMeq}} & 0 & \frac{L_s}{L_{IMeq}} & 0 \\ 0 & \frac{-L_m}{L_{IMeq}} & 0 & \frac{L_s}{L_{IMeq}} \end{bmatrix}, \quad (5)$$

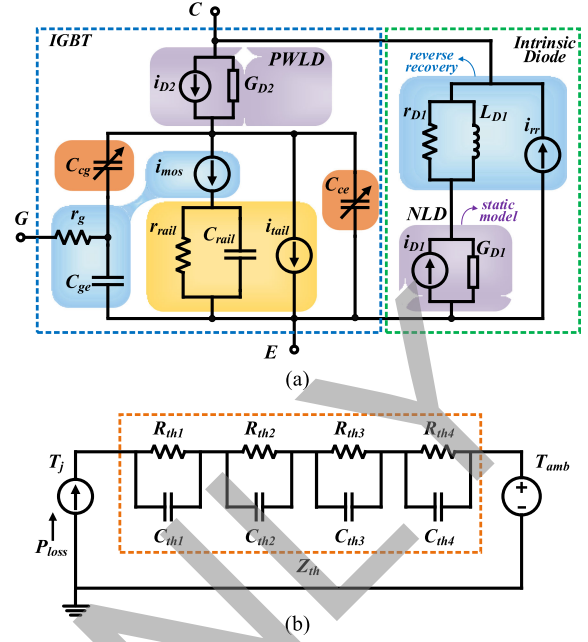


Fig. 3. The device model of IGBT and diode: (a) Nonlinear behaviour model of IGBT and diode, (b) Foster equivalent circuit of thermal network.

where R_s and R_r are the stator and rotor resistances, respectively. ω_r is the electrical angular velocity of the rotor, which is calculated as

$$\omega_r = \frac{P_{req}}{J} \int (T_e - T_m) d\tau, \quad (6)$$

where P_{req} is required power by EV, J is the inertia coefficient, T_e is the electrical torque, and T_m is the mechanical torque.

C. Nonlinear Behaviour Model of IGBT and Diode Pair

The IGBT is one of the essential components of the power converters. The NBM is implemented to represent the physical characteristics of IGBT, i.e., electrothermal performance. As shown in Fig. 3, the NBM can be separated as the IGBT part and diode part. The diode is essential for power converters' regular operation by providing a natural freewheel path for reverse current flow when the IGBT is off. Only static features and the reverse recovery dynamics of the intrinsic diode are considered in the device-level model, and the other parts in the original full behavioural model are ignored in this work.

1) *Diode Nonlinear Behaviour Model*: The nonlinear diode model exhibits static characteristics and reverse recovery features. Fig. 3(a) shows the Norton equivalent circuit of the diode, where the static characteristics are represented by the nonlinear diode (NLD) and the remaining three components are in charge of the reverse recovery process.

The basic relationship between the static current i_{D1} and the junction voltage V_{jD1} takes an exponential form as

$$i_{D1} = i_{sD1} \left(e^{\frac{V_{jD1}}{V_{bD1}}} - 1 \right), \quad (7)$$

where i_{sD1} is the saturation current, and V_{bD1} the junction barrier potential. Discretization and linearization toward this nonlinear

component are carried out, so the conductance G_{D1} and the equivalent current I_{jD1}^{eq} are

$$G_{D1} = \frac{\partial i_{D1}}{\partial V_{jD1}} = \frac{i_{sD1}}{V_{bD1}} e^{\frac{V_{jD1}}{V_{bD1}}}, \quad (8)$$

$$I_{jD1}^{eq} = i_{D1} - G_{D1} V_{jD1}, \quad (9)$$

The reverse recovery phenomenon of the diode is represented by the resistance r_{Ld} parallel-connected with the inductance L_d , and the current source i_{rr} . The Backward Euler integration is adopted for the discretization of inductance due to its lower latency in hardware implementation. The Norton equivalent circuit of the linear inductance L_d is obtained by

$$I_{L_d}(t) = I_{L_d}(t - \Delta t) + \frac{L_d}{\Delta t} V_{L_d}(t), \quad (10)$$

where Δt is the simulation time interval. The voltage controlled current source i_{rr} is proportional to the its voltage as

$$i_{rr} = K_{rr} V_{rr}, \quad (11)$$

where K_{rr} is the constant coefficient of the reverse recovery.

2) *IGBT Nonlinear Behaviour Model*: The nonlinear behaviour model of the IGBT is implemented to demonstrate the sophisticated dynamic characteristics of switches involved in the device-level simulation. As shown in Fig. 3(a), the current source i_{mos} and the capacitor between gate and emitter C_{ge} as well as the capacitor between the collector and the gate C_{cg} are introduced to represent the dynamic behaviour of MOSFET transistor. The inherent gate resistance r_g reflects the static resistance of IGBT.

According to three operating status of IGBT, which are OFF state, the ON state, and the transient state, i_{mos} is defined as a piecewise form with three parts which are

$$i_{mos} = \begin{cases} 0, & V_{cge} \leq V_{ch} \ \& \ V_d \leq 0, \\ a_2 V_d^{(z+1)} - b_2 V_d^{(z+2)}, & V_d < (y \Delta V_{cge})^{\frac{1}{x}}, \\ \frac{\Delta V_{cge}^2}{(a_1 + b_1 \Delta V_{cge})}, & otherwise. \end{cases} \quad (12)$$

where a_1, b_1, a_2, b_2, x, y and z are constant coefficients. These IGBT parameters are listed in appendix, which are obtained since characterizing the device-level switch model is one of the features in SaberRD [29]. V_d is the voltage over i_{mos} . The voltage deviation ΔV_{cge} determines the operating status of IGBT, which is defined as

$$\Delta V_{cge} = V_{cge} - V_{ch}, \quad (13)$$

where V_{cge} is the voltage over capacitor C_{ge} , and V_{ch} is the constant channel threshold voltage.

Considering the three operating states of IGBT, the component yields conductance G_{mosvd} and conductance $G_{mosvcge}$ are respectively derived by taking partial derivatives with respect to ΔV_{cge} .

(1) At OFF stage, V_{cge} is larger than the channel threshold voltage and V_d is lower than or equal to zero. At this time, both G_{mosvd} and $G_{mosvcge}$ are zero.

Distinctly, the tailing current phenomenon which is represented by resistance r_{tail} , capacitance C_{tail} , and tailing current i_{tail} , appears during the turn-off process. The tailing current can be calculated by

$$i_{tail} = \begin{cases} 0, & \frac{V_{tail}}{r_{tail}} < I_{mos}, \\ \left(\frac{V_{tail}}{r_{tail}} - I_{mos} \right) I_{rat}, & otherwise. \end{cases} \quad (14)$$

where V_{tail} is the voltage over C_{tail} .

(2) At On stage, when V_d is lower than $(y \Delta V_{cge})^{\frac{1}{x}}$, the yields conductance can be calculated by

$$G_{mosvd} = a_2(z+1)V_d^z - b_2(z+2)V_d^{(z+1)}, \quad (15)$$

and the conductance is

$$G_{mosvcge} = a_3 V_d^{(z+1)} - b_3 V_d^{(z+2)}. \quad (16)$$

where a_3 and b_3 are constant coefficients.

(3) During the transient stage, V_d is larger than $(y \Delta V_{cge})^{\frac{1}{x}}$, the yields conductance G_{mosvd} is zero, while the conductance is

$$G_{mosvcge} = \frac{2 \Delta V_{cge}}{a_1 + b_1 \Delta V_{cge}} - \frac{b_1 \Delta V_{cge}^2}{(a_1 + b_1 \Delta V_{cge})^2}. \quad (17)$$

The Norton equivalent current I_{mos}^{eq} can be expressed by the following combination:

$$I_{mos}^{eq} = I_{mos} - G_{mosvd} V_d - G_{mosvcge} V_{cge}, \quad (18)$$

PWLD represents the piecewise linear diode at the collector of IGBT with two operating modes. The PWLD model is defined as

$$I_{pwld}^{eq} = -G_{D2} V_{jD2}, \quad (19)$$

where I_{pwld}^{eq} , G_{D2} , and V_{jD2} are the equivalent current and conductance, and junction voltage of PWLD, respectively. G_{D2} can be deemed as a binary conductor whose value varies with on- and off-state.

Thus, the discrete model of IGBT can be derived using the IGBT nodal voltage \mathbf{V}_p and current source \mathbf{I}_p contribution as

$$\mathbf{Y}_p \cdot \mathbf{V}_p = \mathbf{I}_p, \quad (20)$$

where the admittance matrix \mathbf{Y}_p is a 5×5 dimension.

3) *IGBT Electro-Thermal Model*: In order to reveal thermal information on IGBT and diode pair, the foster transient electro-thermal impedance model [30] is introduced with the resistor $R_{th}^{(i)}$ and capacitor $C_{th}^{(i)}$. As an integral part of the switching device, the electro-thermal model takes the following form of

$$Z_{th} = \sum_{i=1}^4 R_{th}^{(i)} \left(1 - e^{-\frac{t}{\tau_i}} \right), \quad (21)$$

where τ_i is time constant. The IGBT power loss produces heat during the power converter operation. Accordingly, the power loss P_{loss} is the input to the current source whose terminal voltage is represented to the semiconductors junction temperature T_j

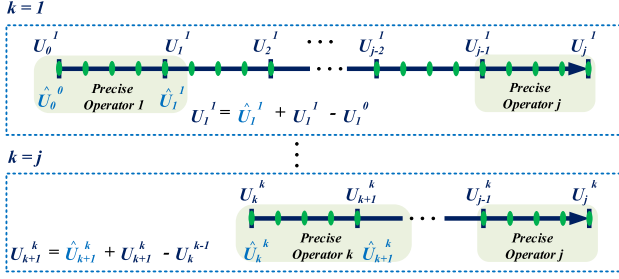


Fig. 4. Iteration procedures of the proposed parallel-in-time for EMT simulation.

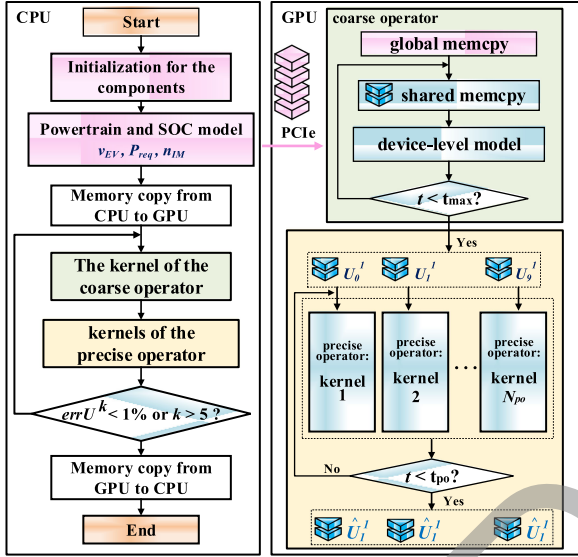


Fig. 5. GPU kernels design for parallel-in-time EMT simulation of EV.

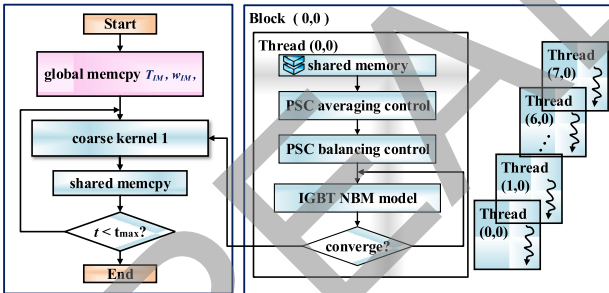


Fig. 6. Flowchart of a single kernel for device-level simulation.

as shown in Fig. 3(b). The junction temperature can be calculated based on

$$T_{vj}(t) = \sum_{i=1}^N \frac{P_{loss}(t)}{G_{ci} + \frac{1}{R_{th}^{(i)}}} + T_{amb}, \quad (22)$$

where T_{amb} represents the ambient temperature, which is 25°C in this paper. T_j is then used to update the temperature-dependent parameters of NBM.

III. SYSTEM-LEVEL MODELING OF MMC-BASED EVS

Fig. 1 shows the configuration of a three-phase MMC using half-bridge submodules in the energy system of EVs. Each

phase contains two arms, which constitute an inductance and N submodules for attaining $N + 1$ voltage levels.

A. MMC Modeling

The advantages of MMC, including strong harmonic suppression and fault blocking capability, are given by the modular construction where each half-bridge converter is considered as a submodule. As shown in Fig. 1, submodules are physically independent with two nodes and connected in series in each branch. Thus, an arbitrary submodule can be solved simultaneously, and the output of each submodule can be synthesized based on the primary circuit of MMC.

The half-bridge submodule corresponds to an eight-dimensional matrix where IGBT and diode pair has five nodes. The admittance matrix and the current vector of the submodule are constructed as

$$\mathbf{G}_{sm} = \begin{bmatrix} \mathbf{G}_{5 \times 5}^{pu} & \mathbf{0} \\ \mathbf{0} & \mathbf{0} \end{bmatrix}_{8 \times 8} + \begin{bmatrix} G_{cap} & \mathbf{0} \\ \mathbf{0} & \mathbf{G}_{4 \times 4}^{pd} \end{bmatrix}_{8 \times 8}, \quad (23)$$

where \mathbf{G}^{pu} and \mathbf{G}^{pd} are the conductance matrices of IGBT and diode pair at the upper arm and lower arm, respectively. G_{cap} is the conductance of the capacitance of half-bridge. In addition, the current contribution of a submodule takes the form of

$$\mathbf{I}_{sm} = \begin{bmatrix} \mathbf{I}_{5 \times 1}^{pu} \\ \mathbf{0}_{3 \times 1} \end{bmatrix} + \begin{bmatrix} \mathbf{0}_{4 \times 1} \\ \mathbf{I}_{4 \times 1}^{pd} \end{bmatrix} + \begin{bmatrix} I_{c1} \\ \mathbf{0}_{7 \times 1} \end{bmatrix}. \quad (24)$$

As shown in Fig. 1, the eighth node of lower IGBT is regarded as the virtual ground so that elements related to the ground node are zeros.

In this work, the phase shift control (PSC) is adopted for the regulation of MMC according to [28]. The MMC main circuit turns out to be linear after being separated as N submodules. The arm, composed of voltage sources coupled to the submodules and the inductance, can be expressed as

$$U_{arm} = (I_{arm} - I_{req})Z_{arm} + \sum_{i=1}^N u_{smi}, \quad (25)$$

where U_{arm} and I_{arm} are arm voltage and current respectively. u_{smi} is the capacitance voltage of i th submodule. The main circuit having a direct connection to the IM, therefore, both the MMC and IM have to be solved together from the perspective of the system-level simulation of EVs.

B. Powertrain Modeling

In order to achieve the system-level simulation of the energy system under the conditions of different speed profiles, the powertrain model of the EV is required to build the relationship between the vehicle speed and the energy and power requirement from the battery energy storage system and the IM, respectively.

The EV dynamics is modeled as a mass and a set of propulsion and resistance forces [13], [31], which include the power of acceleration force F_{acc} , the power from tire rolling resistance and aerodynamic resistance F_{res} , and the power of gravitational resistance by the slope in the road F_{gx} . If the speed and mass of EV are respectively noted as v_{ev} and m_{ev} , three types of

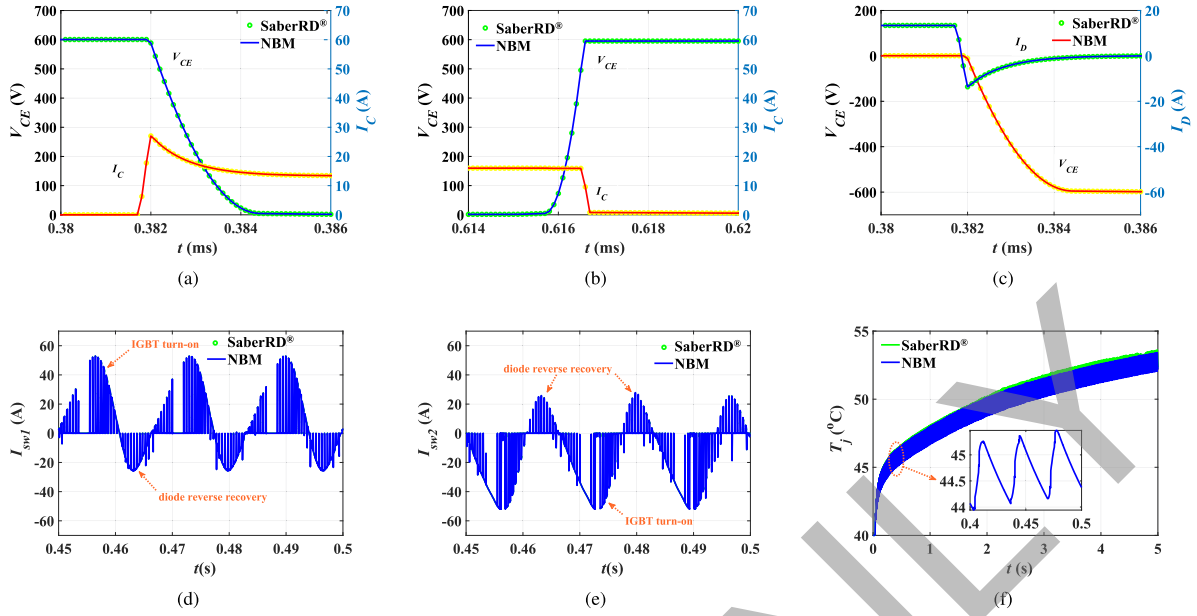


Fig. 7. Switching transients behaviour, patterns and junction temperature of IGBT/diode pair: (a) Turn-on, (b) turn-off, (c) diode reverse recovery, (d) switch 1 current, (e) switch 2 current, and (f) IGBT junction temperatures.

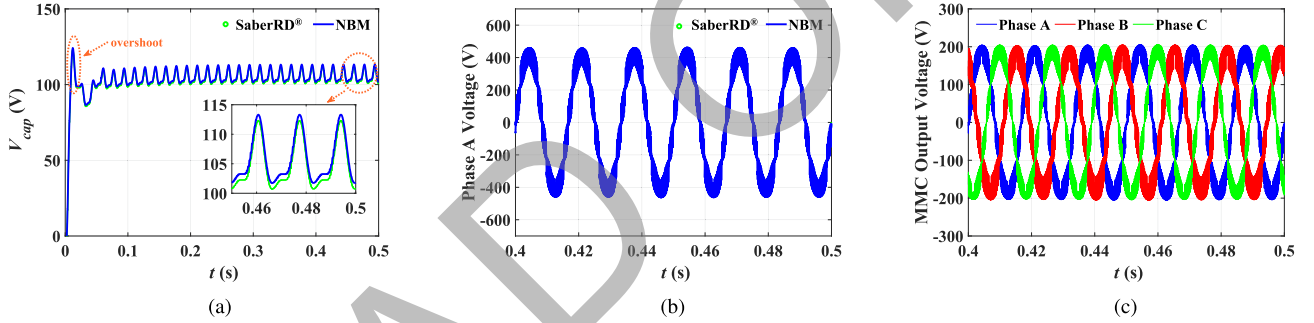


Fig. 8. MMC voltage and currents: (a) Capacitance voltage of the first submodule, (b) phase A voltage, (c) three-phase MMC voltage output.

resistances can be calculated according to the following equation

$$\begin{aligned} F_{acc} &= m_{ev} a_{ev}(t), F_{gx} = m_{ev} g \sin(\beta), \\ F_{res} &= C_{r, ev} m_{ev} g \cos(\beta) + \frac{1}{2} \rho C_{ae, ev} A_F v_{ev}^2(t), \end{aligned} \quad (26)$$

where a_{ev} is the accelerated speed of the EV, g is the acceleration of gravity, β is the slope of the roadway, C_r is the coefficients of the rolling resistance, ρ is the air density, C_{ae} is the penetration air coefficient, and A_F is the front area of EV.

The required power from the EV, which overcomes the resistances force of the EV, can be calculated by

$$F_{load} = F_{acc} + F_{res} + F_{gx}. \quad (27)$$

Then the requested energy from batteries is calculated by integrating the vehicle power over the time according to the following equation:

$$E_{load} = \int_0^t P_{load} d\tau = \int_0^t F_{load} \cdot v_{ev}(\tau) d\tau. \quad (28)$$

In addition, if the gearbox coefficient is denoted as η_{gr} , the speed relationship between IM and EV is

$$n_{im} = \eta_{gr} v_{ev}. \quad (29)$$

Then the IM speed can be obtained from the vehicle speed profiles.

C. Energy Management Strategy

In Fig. 1, a double-loop control-based energy management strategy is designed in this paper. There are two operating modes: the charging mode and the discharging mode determined by battery current.

Besides, a PI-based double loop controller is used for regulating the power converter of the battery energy storage system. The outer controller is the voltage controller whose input is the error between bus voltage reference and the measurements to maintain the bus voltage. Besides, the inner controller is the current controller, which follows the load currents. The voltage control loop's response is slower than that of the current control

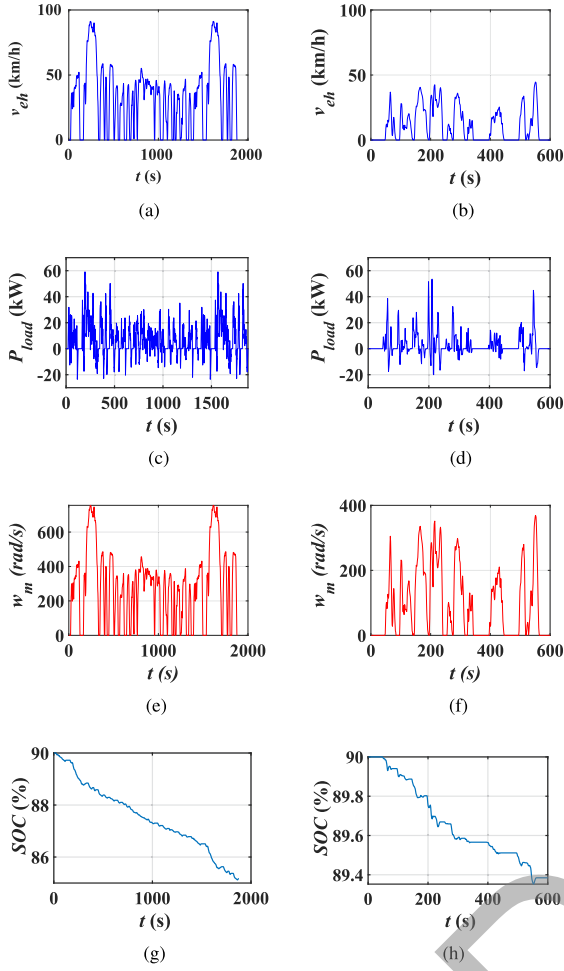


Fig. 9. Speed, power and energy curves from EPA and NYCC driving cycle: (a) EPA vehicle speed, (b) NYCC vehicle speed, (c) EPA power requirement, (d) NYCC power requirement, (e) EPA angular velocity, (f) NYCC angular velocity, (g) SOC curves for one EPA cycle, (h) SOC curves for one NYCC cycle.

loop; therefore, the bandwidth of the voltage control loop is chosen lesser than that of the current control loop.

IV. PARALLEL-IN-TIME IMPLEMENTATION FOR MMC-BASED ENERGY SYSTEM

The complexity in the device-level simulation for the energy system of EVs mainly comes from the power electronics. hence, it is important to develop a fast simulation method to reduce the simulation time cost. The parallel algorithm belongs to the class of temporal decomposition methods which divide the time interval into sub-intervals and solve them concurrently. An interpolation strategy is developed based on the parallel-in-time algorithm, which is implemented at an arbitrary moment of the device-level simulation with the nanosecond-level time interval.

A. Parallel-in-Time-Based Interpolation Strategy

It is straightforward to increase the time-step for accelerating the power system dynamic simulations. However, the twofold goals of convergence time reduction and the high accuracy of the device-level model cannot be achieved when the time-step

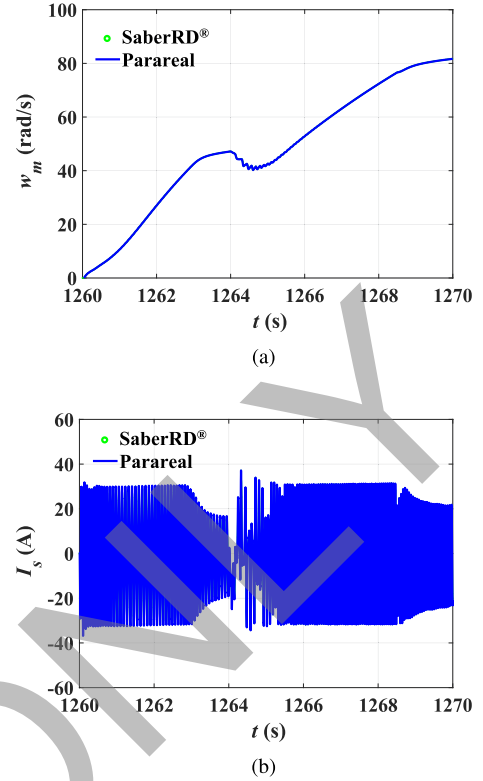


Fig. 10. System-level simulation results: (a) Angular velocity curves of IM, and (b) MMC Phase A current.

increased. Thus, the parallel-in-time algorithm was introduced to accelerate the EV simulation. The basic concept of a parallel-in-time algorithm is to divide the time evolution problem into a series of independent evolution problems on smaller time intervals based on numerical analysis theory.

Generally, the parallel-in-time algorithm requires at least two operators: the coarse operator and the precise operator. In this work, device-level models are involved in parallel-in-time operators. The coarse operator works in a larger time-step ΔT , while multiple precise operators work in a smaller time-step Δt .

The solutions of coarse and precise operators are respectively defined as:

$$\begin{aligned} \text{Coarse} : \hat{U}_j^k &= F(t_j, \Delta t, \hat{U}_{j-1}^{k-1}), \\ \text{Precise} : U_j^k &= G(T_j, \Delta T, U_{j-1}^{k-1}), \end{aligned} \quad (30)$$

where k is the iteration number of the parallel-in-time algorithm, \hat{U}_j^k and U_j^k are the solution of system ODE from the coarse and the precise operator, respectively. For the coarse operator, the operating time is equal to the simulation time. While, for the precise operator, the operating time is from T_{j-1} to T_j . Thus, the whole simulation time from t_0 to t_{max} is decomposed into N_{max} window intervals, and the j th window is started from T_{j-1} to T_j . In addition, the running time of single precise operator is $t_{po} = \frac{\Delta T}{\Delta t}$.

According to [32], the system-level equations can be defined as

$$U_j - F(t_j, t_{j-1}, \hat{U}_{j-1}) = 0, \quad (31)$$

where U_j is the solution by parallel-in-time method. The system equations can be solved by Newton-Raphson method according to

$$U_j^k = \widehat{U}_j^k + \frac{\partial \widehat{U}_j^k}{\partial U} \Delta U_{j-1}^k, \quad (32)$$

where $\Delta U_{j-1}^k = U_{j-1}^k - U_{j-1}^{k-1}$. U_{j-1}^k is the system output at k th iteration.

Because both the coarse and the precise operator use the same model and system parameters, \widehat{U}_j^k and U_j^k are approximately the same with the acceptable error. Based on the backward differentiation formula, the partial differential item in equation (32) can be approximately obtained by

$$\frac{\partial F}{\partial U} = \frac{\widehat{U}_j^k - \widehat{U}_j^{k-1}}{U_{j-1}^k - U_{j-1}^{k-1}}. \quad (33)$$

Thus, when substituting the assumption into system equations (31), the solution by parallel-in-time algorithm can be obtained by

$$U_j^k = \widehat{U}_j^k + U_j^k - U_j^{k-1}. \quad (34)$$

Notice that the parallel-in-time method is differentiated by the iteration number index k not the time-step j . As shown in Fig. 4, the solution process starts from $t = 0$ time step, when $k = 1$. The coarse operator provides the initial value of \widehat{U}_j^k for precise operator iteratively. N_{po} precise operators are running in parallel from the perspective of time with time-step of Δt .

B. Parallel-in-Time Simulation of EV Power System

The parallel-in-time algorithm is implemented in device-level simulation due to the computation burden is mainly caused by the solution process for MMC. Fig. 5 shows the parallel-in-time design in GPU kernels. The powertrain model generates the IM speed, and the SOC model calculates the required power in the CPU. Then these data and global variables are sent to GPU through PCIe bus.

The first value U_0^0 of MMC and IM at $k = 0$ is assumed known at the beginning. The coarse operator is initialized with the system states U_0 with the time-step with $\Delta T = 100$ ns.

Meanwhile, there are multiple precise operators to solve the system ODE at the time-step of Δt in a parallel manner. Each precise operator is programmed as a grid which is also known as a kernel, which simulates the output voltage and current of MMC, the output power, and the inner variables of IGBT and diode pairs using the initial values from the coarse operator.

For each kernel, there are eight threads of parallelism, which is the same as the number of arms in the MMC. As shown in Fig. 6, each thread is designed to solve the dynamics of individual arms including phase-shift control and the NBM model of IGBT and diode pair.

Finally, the device-level parallel-in-time simulation results are available based on equation (34) using the solution vectors of coarse operators and precise operators. The deviation between

TABLE II
PARAMETERS OF TESLA X 75D [34]

Parameters	Value	Parameters	Value
Engine power	193 kW	m_{ev}	2352 kg
Engine torque	329 Nm	$C_{r,ev}$	0.02
Battery capacity	75 kWh	$C_{ae,ev}$	0.24
Range EPA	381 km	η_{gr}	8.2752

U^k and U^{k-1} is calculated by

$$errU^k = \sum_{j=k}^{Num_1} \frac{\|U_j^k - U_j^{k-1}\|}{\|U_j^k\|}. \quad (35)$$

In this work, $errU^k$ is expected to less than 1%.

The parallel-in-time implementation in device-level simulation for power systems generally requires 4 GB of memory and 100 GB/s bandwidth between CPU and GPU. For a specific MMC (e.g., five-level), at least 100 GPU cores are used for the proposed parallel-in-time method.

V. SIMULATION RESULTS AND DISCUSSION

The device-level simulation was carried out on both CPU and GPU on the 2.2 GHz Intel Xeon E5-2698 v4 CPU and 192 GB RAM. The GPU configuration is the Nvidia Tesla V100 with 5120 CUDA cores, 16 GB of memory whose bandwidth is 900 GB/s [33]. In addition, the system-level simulation results are validated by the datasheet of the Tesla Model X 75D whose parameters as listed in Tab. II.

A. Device-Level Switching Transients

The switching transients of IGBT/diode pair from five-level MMC with the DC bus voltage of 400 V are provided in Fig. 7. The gate voltage is ± 15 V and the gate resistance is 10 Ω . With the dead-time of 5 μ s and switching frequency of 4 kHz, the turn-on current of IGBT overshoots lightly at around 0.382 ms. During the turn-off period, V_{CE} increased from 0 V to 600 V, which is the same as V_{CE} from the datasheet. Fig. 7(c) shows the diode reverse recovery process.

Figs. 7(d) and 7(e) show the upper and lower switch currents of one submodule. When the IGBT turns on, the switch current is changed according to the submodule currents, while when the IGBT turn-off the switch current increased in the reverse direction which accounts for the diode reverse recovery. In the Fig. 7(f), the junction temperature of the IGBT suddenly surges when the MMC starts to operate, and the curve decreases gradually along with the steady-state of MMC. Simulation is also conducted in the commercial EMT tool to validate the NBM of IGBT and diode pair and the designed MMC GPU kernel.

Fig. 8 shows the MMC output voltage with the source frequency of 60 Hz, the submodule capacitor of 6 m Ω , and the arm inductance of 1 mH. Fig. 8(a) demonstrates the capacitor voltage in the first submodule of the upper arm. Since the DC voltage is 400 V, the capacitor voltage reference for individual submodules in the five-level MMC is expected to be 100 V. Fig. 8(a) shows the voltage overshoot during the MMC start-up, with the maximum value of 132.1 V, and eventually remains at

TABLE III
EXECUTION TIME AND SPEED-UP OF EV SIMULATION FOR 10 s DURATION

Time-step (ns)	Execution Time ($\times 10^2$ s)				Parallel-in-time Speed-up		Max. Memory (MB)	
	CPU	GPU	Parallel-in-time (10 kernels)	Parallel-in-time (30 kernels)	10 kernels	30 kernels	CPU	GPU
10	84.31	78.35	19.06	12.72	4.11	6.16	1081	1256
40	31.57	24.56	8.62	6.88	2.85	3.57	786	846
80	22.67	18.87	7.63	6.55	2.47	2.88	571	691

100 V at steady-state. The phenomenon in the zoomed-in figure is also caused by the diode reverse recovery. The single-phase voltage and three-phase voltage of MMC are shown in Figs. 8(b) and 8(c). The accuracy of these results is validated by SaberRD.

B. System-Level Simulation for EVs

As is well known, different types of EVs have been recently designed with a wide capacity of driving range. As shown in Fig. 7, the speed profiles of Environmental Protection Agency (EPA) urban dynamometer driving schedule and the New York City Cycle (NYCC) [13] are chosen for the system-level testing.

Figs. 9(a) and 9(b) show v_{eh} from EPA and NYCC, respectively, using which the load power and angular velocity can be calculated using the powertrain model. Figs. 9(g) and 9(h) demonstrate the SOC variation along with the EPA and NYCC cycles.

Fig. 10 provides the five-level MMC connected with the IM responses to the vehicle speed variation from 60 s to 70 s under the condition of the EPA driving cycle. The angular velocity increased to 51.2 rd/s, then gradually decreased started at about 64 s. During this period, the current of MMC phase A decreased at around 63 s when the rate of the angular velocity changing decreased. During 65 s to 70 s, ω_m keeps increasing, while the rate varies with time after 68 s.

Table III summarizes the execution times, the parallel-in-time speed-up, and maximum used memory for device-level simulation of EV in different time steps. The test is conducted on the five-level MMC at the switching frequency of 4 kHz during 10 s. The results show that the GPU processor takes less time than CPU simulation since the submodules of MMC are processed in a parallel manner in several threads. The proposed parallel-in-time simulation can significantly reduce the execution time using 10 kernels and 30 kernels. Table III shows that the proposed parallel-in-time interpolation strategy significantly accelerates the device-level and system-level MMC-based EV simulation.

Furthermore, the parallel-in-time performs better when the precise time-step becomes smaller, because more nonlinear solution procedures can be processed in a parallel manner. In other word, the larger the difference between the operator's time interval, the more significantly the proposed method performs. However, the time step of coarse operator cannot be too large, which will cause the convergence problem of device-level simulation. Moreover, with the increasing kernel number of precise operators, the proposed method requires less execution time.

VI. CONCLUSION

In this paper, a parallel-in-time device-level simulation method is proposed for the MMC-based power system of EVs. The NBM can reveal thermal information and EMT behavior during the MMC operation, which is essential for the design of energy management strategy and EVs testing. Particularly, an interpolation strategy is designed based on the parallel-in-time algorithm to reduce the simulation execution time with the two operators working at different time-step. The proposed interpolation strategy can significantly speed up the device-level simulation by processing the nonlinear solution procedures in precise operators in a parallel manner, using the coarse operators' initial values. The simulation results show that system-level EMT simulation involving NBM of IGBT and diode pair is feasible when the parallel-in-time algorithm is utilized. The simulation execution time shows that the proposed parallel-in-time simulation method can speed up the device-level simulation of EVs. Future research will extend the approach to achieve a comprehensive multi-domain simulation of EVs.

APPENDIX

The Siemens BSM300GA160D IGBT behavioral model parameters $i_{sD1} = 0.01$, $L_{D1} = 10^{-11}$ H, $r_{D1} = 12.8 \mu\Omega$, $V_{bD1} = 0.1495$, $K_{rr} = 9874.1$, $V_{ch} = 6.3$ V, $a_1 = 0.022$, $b_1 = 0.004$, $a_2 = 92.5129$, $b_2 = 4.0188$, $a_3 = -0.1943$, $b_3 = -0.4827$, $x = 0.974$, $y = 1.429$, $z = 0.369$, $r_{tail} = 1 \mu\Omega$, $C_{tail} = 10$ F.

REFERENCES

- [1] A. Hintz, U. R. Prasanna, and K. Rajashekara, "Novel modular multiple-input bidirectional DCDC power converter (MIPC) for HEV/FCV application," *IEEE Trans. Ind. Electron.*, vol. 62, no. 5, pp. 3163–3172, May 2015.
- [2] M. Quraan, P. Tricoli, S. D'Arco, and L. Piegari, "Efficiency assessment of modular multilevel converters for battery electric vehicles," *IEEE Trans. Power Electron.*, vol. 32, no. 3, pp. 2041–2051, Mar. 2017.
- [3] M. Narimani, B. Wu, and N. R. Zargari, "A novel five-level voltage source inverter with sinusoidal pulse width modulator for medium-voltage applications," *IEEE Trans. Power Electron.*, vol. 31, no. 3, pp. 1959–1967, Mar. 2016.
- [4] W. Yang, Q. Song, S. Xu, H. Rao, and W. Liu, "An MMC topology based on unidirectional current H-bridge submodule with active circulating current injection," *IEEE Trans. Power Electron.*, vol. 33, no. 5, pp. 3870–3883, May 2018.
- [5] C. Gan, Q. Sun, J. Wu, W. Kong, C. Shi, and Y. Hu, "MMC-based SRM drives with decentralized battery energy storage system for hybrid electric vehicles," *IEEE Trans. Power Electron.*, vol. 34, no. 3, pp. 2608–2621, Mar. 2019.
- [6] D. Ronanki and S. S. Williamson, "Modular multilevel converters for transportation electrification: Challenges and opportunities," *IEEE Trans. Transport. Electric.*, vol. 4, no. 2, pp. 399–407, Jun. 2018.

- [7] A. Salem and M. Narimani, "A review on multiphase drives for automotive traction applications," *IEEE Trans. Transport. Electrification*, vol. 5, no. 4, pp. 1329–1348, Dec. 2019.
- [8] D. Gao, C. Mi, and A. Emadi, "Modeling and simulation of electric and hybrid vehicles," *Proc. IEEE*, vol. 95, no. 4, pp. 729–745, Apr. 2007.
- [9] Y. Zhang, S. Lu, Y. Yang, and Q. Guo, "Internet-distributed vehicle-in-the-loop simulation for HEVs," *IEEE Trans. Veh. Technol.*, vol. 67, no. 5, pp. 3729–3739, May 2018.
- [10] C. M. Martinez, X. Hu, D. Cao, E. Velenis, B. Gao, and M. Wellers, "Energy management in plug-in hybrid electric vehicles: Recent progress and a connected vehicles perspective," *IEEE Trans. Veh. Technol.*, vol. 66, no. 6, pp. 4534–4549, Jun. 2017.
- [11] Y. Lee, A. Khaligh, and A. Emadi, "Advanced integrated bidirectional AC/DC and DC/DC converter for plug-in hybrid electric vehicles," *IEEE Trans. Veh. Technol.*, vol. 58, no. 8, pp. 3970–3980, Oct. 2009.
- [12] L. Li, B. Yan, C. Yang, Y. Zhang, Z. Chen, and G. Jiang, "Application-oriented stochastic energy management for plug-in hybrid electric bus with AMT," *IEEE Trans. Veh. Technol.*, vol. 65, no. 6, pp. 4459–4470, Jun. 2016.
- [13] T. Mesbahi, F. Khenfri, N. Rizoug, P. Bartholomeus, and P. L. Moigne, "Combined optimal sizing and control of li-ion battery/supercapacitor embedded power supply using hybrid particle swarmeldermead algorithm," *IEEE Trans. Sustain. Energy*, vol. 8, no. 2, pp. 59–73, Jan. 2017.
- [14] R. Xiong, Y. Zhang, J. Wang, H. He, S. Peng, and M. Pecht, "Lithium-ion battery health prognosis based on a real battery management system used in electric vehicles," *IEEE Trans. Veh. Technol.*, vol. 68, no. 5, pp. 4110–4121, May 2019.
- [15] J. Yang, B. Xia, Y. Shang, W. Huang, and C. C. Mi, "Adaptive state-of-charge estimation based on a split battery model for electric vehicle applications," *IEEE Trans. Veh. Technol.*, vol. 66, no. 12, pp. 10889–10898, Jul. 2017.
- [16] B. J. Baliga, "Analytical modeling of IGBTs: Challenges and solutions," *IEEE Trans. Electron Devices*, vol. 60, no. 2, pp. 535–543, Feb. 2013.
- [17] A. S. Bahman, K. Ma, P. Ghimire, F. Iannuzzo, and F. Blaabjerg, "A 3-D-lumped thermal network model for long-term load profiles analysis in high-power IGBT modules," *IEEE J. Emerg. Sel. Topics Power Electron.*, vol. 4, no. 3, pp. 1050–1063, Sep. 2016.
- [18] N. Lin and V. Dinavahi, "Exact nonlinear micromodeling for fine-grained parallel EMT simulation of MTDC grid interaction with wind farm," *IEEE Trans. Ind. Electron.*, vol. 66, no. 8, pp. 6427–6436, Aug. 2019.
- [19] R. Zhu, N. Lin, V. Dinavahi, and G. Liang, "An accurate and fast method for conducted EMI modeling and simulation of MMC-based HVDC converter station," *IEEE Trans. Power Electron.*, vol. 35, no. 3, pp. 4689–4702, May 2020.
- [20] S. Esmaeili and S. Kouhsari, "A distributed simulation based approach for detailed and decentralized power system transient stability analysis," *Electr. Power Syst. Res.*, vol. 77, no. 5–6, pp. 673–684, Apr. 2007.
- [21] M. Tomim, J. Marti, and L. Wang, "Parallel solution of large power system networks using the Multi-Area Thévenin Equivalents (MATE) algorithm," *Int. J. Electr. Power Energy Syst.*, vol. 31, no. 9, pp. 497–503, Sep. 2009.
- [22] G. Gurrula, A. Dimitrovski, S. Pannala, S. Simunovic, and M. Starke, "Parallel in time for fast power system dynamic simulations," *IEEE Trans. Power Syst.*, vol. 31, no. 3, pp. 1820–1830, May 2016.
- [23] Y. Song and B. Wang, "Analysis and experimental verification of a fault-tolerant hev powertrain," *IEEE Trans. Power Electron.*, vol. 28, no. 12, pp. 5854–5864, Feb. 2013.
- [24] P. Igetic, "Exponential ade solution based compact model of planar injection enhanced IGBT dedicated to robust power converter design," *IEEE Trans. Power Electron.*, vol. 30, no. 4, pp. 1914–1924, Apr. 2015.
- [25] N. Lin and V. Dinavahi, "Variable time-stepping modular multilevel converter model for fast and parallel transient simulation of multiterminal DC grid," *IEEE Trans. Ind. Electron.*, vol. 66, no. 9, pp. 6661–6670, Sep. 2019.
- [26] M. Khayamy, A. Nasiri, and O. Okoye, "Development of an equivalent circuit for batteries based on a distributed impedance network," *IEEE Trans. Veh. Technol.*, vol. 69, no. 6, pp. 6119–6128, Apr. 2020.
- [27] J. Xu, C. C. Mi, B. Cao, J. Deng, Z. Chen, and S. Li, "The state of charge estimation of lithium-ion batteries based on a proportional-integral observer," *IEEE Trans. Veh. Technol.*, vol. 63, no. 4, pp. 1614–1621, May 2014.
- [28] P. Krause, O. Wasynczuk, S. Sudhoff, and S. Pekarek, *Analysis of Electric Machinery and Drive Systems*. Hoboken, NJ, USA: Wiley.
- [29] S. Inc., *Saber Model Architect Tool User Guide*, USA, Sep. 2009.
- [30] N. Lin, P. Liu, and V. Dinavahi, "Component-level thermo-electromagnetic nonlinear transient finite element modeling of solid-state transformer for DC grid studies," *IEEE Trans. Ind. Electron.*, vol. 68, no. 2, pp. 938–948, Feb. 2021.
- [31] R. E. Araujo, R. Castro, C. Pinto, P. Melo, and D. Freitas, "Combined sizing and energy management in EVs with batteries and supercapacitors," *IEEE Trans. Veh. Technol.*, vol. 63, no. 7, pp. 3062–3076, Sep. 2014.
- [32] T. Cheng, T. Duan, and V. Dinavahi, "Parallel-in-time object-oriented electromagnetic transient simulation of power systems," *IEEE Open Access J. Power Energy*, vol. 7, pp. 296–306, Jul. 2010.
- [33] NVIDIA Tesla V100 GPU Architecture, Aug. 2017. [Online]. Available: <https://images.nvidia.com/content/volta-architecture/pdf/volta-architecture-whitepaper.pdf>
- [34] Tesla Model X 75D, Jan. 2018. [Online]. Available: <https://www.guideautoweb.com/en/makes/tesla/model-x/2018/specifications/75/d/>



Chengzhang Lyu (Graduate Student Member, IEEE) received the B.Sc. and M.Sc. degrees from Central South University, Changsha, China, in 2016 and 2019. He is currently working toward the Ph.D. degree with the Department of Electrical and Computer Engineering, University of Alberta, Edmonton, AB, Canada. His current research interests include electromagnetic transient simulation of power and energy systems, device-level modeling, electric vehicles, power electronics, parallel and distributed computing, and real-time simulation.



Ning Lin (Member, IEEE) received the B.Sc. and M.Sc. degrees in electrical engineering from Zhejiang University, Hangzhou, China, in 2008 and 2011, respectively, and the Ph.D. degree in electrical and computer engineering from the University of Alberta, Edmonton, AB, Canada, in 2018. From 2011 to 2014, he was an Engineer of flexible AC transmission system and high-voltage direct current transmission. His research interests include electromagnetic transient simulation, transient stability analysis, real-time simulation, device-level modeling, integrated ac-dc grids, massively parallel processing, heterogeneous high-performance computing of power systems, and power electronics.



Venkata Dinavahi (Fellow, IEEE) received the B.Eng. degree in electrical engineering from the Visveswaraya National Institute of Technology, Nagpur, India, in 1993, the M.Tech. degree in electrical engineering from the Indian Institute of Technology Kanpur, Kanpur, India, in 1996, and the Ph.D. degree in electrical and computer engineering from the University of Toronto, ON, Canada, in 2000. He is currently a Professor with the Department of Electrical and Computer Engineering, University of Alberta, Edmonton, AB, Canada. His research interests include real-time simulation of power systems and power electronic systems, electromagnetic transients, device-level modeling, largescale systems, and parallel and distributed computing.